Journal of
Materials Chemistry A

ROYAL SOCIETY
OF **CHEMISTRY**

PAPER

View Article Online
View Journal | View Issue

Check for updates

Cite this: *J. Mater. Chem. A*, 2022, **10**, 2567

Molecular dynamics study of oxygen-ion diffusion in yttria-stabilized zirconia grain boundaries†

Jose Carlos Madrid Madrid,[a] Junko Matsuda,[b] Kwati Leonard,[b]
Hiroshige Matsumoto[b] and Kulbir Kaur Ghuman*[a]

Received 26th September 2021
Accepted 18th January 2022

DOI: 10.1039/d1ta08309k

rsc.li/materials-a

This work focuses on understanding the oxygen-ion transport through the mixed Grain Boundaries (GBs) present in yttria-stabilized zirconia (YSZ), a common solid oxide fuel cells (SOFCs) electrolyte. The mixed GBs, having a disordered arrangement of atoms due to the merging of crystalline facets of the two adjacent grains, were found to be the most prominent in experimentally prepared samples. In this work, all GBs were constructed using the amorphization and recrystallization technique implemented *via* molecular dynamics. An in-depth study was conducted for a mixed GB present in our 8YSZ sample, formed by the planes (−511) and (21−1). Oxygen-ion self-diffusion was studied for a range of temperatures between 700 K and 2300 K and for samples having Y_2O_3 concentration between 4–14 mol%. The oxygen-ion diffusion in the prepared mixed GBs was then compared with the well-investigated high symmetry GBs, *i.e.*, $\Sigma = 5(310)/[001]$, $\Sigma = 11(311)/[110]$, $\Sigma = 13(510)/[001]$, another mixed GB formed by (20−1) and (100) planes and the single-crystal. In agreement with the previous studies, the optimum Y_2O_3 content for maximum oxygen self-diffusion in mixed GB was found to be 8 mol%. Furthermore, it was found that oxygen self-diffusion is hindered not only at the GB core but also inside grains having specific orientations. This is attributed to the formation of oxygen vacancy (V_O) clusters indicated by Y^{3+} segregation and the subsequent lack of O^{-2} ions at the GB core. The collective analysis of this study indicates that at optimum Y_2O_3 concentration, specific grain orientations concerning the GB plane reduce the oxygen vacancy clustering at the grain interior regions close to GB, thereby resulting in the overall higher oxygen-ion diffusivity of the mixed GBs.

1 Introduction

Electrolyte samples are generally polycrystalline with different grain sizes, grain orientations, dopant segregation, and defect distribution. In addition, they are typically characterized by a high density of Grain Boundaries (GBs). All these features can substantially affect ionic conductivity. When two grains meet and create a boundary at a certain angle, the atoms that meet and belong to two different lattice orientations rearrange to obtain the lowest energy structure between the two grains. The rearranging of atoms results in a disordered region of a few atomic layers that separates both grain lattices, the width of which depends on the angle between the two lattices. Consequently, the formation of GBs translates into disorder and in other microstructural defects, such as vacancies or dislocations, in the region of the grain near the GB, due to the stress created by the lattice mismatch of the two grains at their interface. Therefore, it is expected that any phenomenon (such as ion transport), which depends upon the degree of disorder between the two grains, would change based on their coincidence angle. In contrast with other fluorite like materials, in UO_2 doped structures oxygen diffusion at GBs have been reported to not change in comparison to bulk.[1,2] In addition, several computational studies explained how GBs provide fast-channels for oxygen conductivity between different grains in UO_2.[1–6]

Experimentally, the atomistic structure of GBs can be analysed and observed *via* transmission electron microscopy (TEM).[7] However, atomistic and electronic level simulations are usually adopted to fully understand the transport mechanism of oxygen-ions across the grains and GBs. Specifically, Molecular Dynamics (MD) simulation has been the most frequently used approach to study the GBs structure at a larger scale.[8] Over the past 40 years, MD techniques have been mainly applied to simulate the oxygen-ion transport in high symmetry tilt or twist grain boundaries of commonly used solid oxide fuel cells (SOFCs) electrolytes.[9–21] However, since the majority of boundaries found in polycrystalline samples are a mix of twisted and tilted denominations-commonly named as "mixed," "general," or "random" GBs,[22–25] identifying pathways to enhance ion

---

[a] *Institut National de la Recherche Scientifique, Centre Énergie Matériaux Télécommunications, 1650 Boul. Lionel-Boulet, Varennes J3X 1S2, Quebec, Canada. E-mail: Kulbir.Ghuman@inrs.ca*

[b] *International Institute for Carbon-Neutral Energy Research (I2CNER-WPI), Kyushu University, 744 Motooka, Nishi-ku, Fukuoka 819-0395, Japan*

† Electronic supplementary information (ESI) available. See DOI: 10.1039/d1ta08309k

transport through mixed GBs is essential to improve oxygen-ion conductors' performance substantially. Therefore, in this study, an in-depth MD analysis was conducted to investigate the role of mixed GBs in well-known yttria-stabilized zirconia (YSZ) electrolytes. For comparison, we have also studied symmetric or Coincidence Site Lattice (CSL) GBs. CSL GBs are considered to be special within polycrystalline materials. They are believed to be low-energy and high symmetry, and they are observed to be resistant to intergranular fracture in contrast to mixed or general GBs.[26,27] Further, we chose to investigate YSZ as it is not only a benchmark material used in SOFCs since the 1980s due to its excellent mechanical stability and durability, but also because it is a pure ionic conductor with no electronic conductivity, making it a perfect material for conducting this systematic study.

Literature shows extensive and detailed studies on CSL tilted or twisted YSZ GBs, either by computational,[9–21] or experimental[7,16,28–30] approaches. However, to our best knowledge, no work focused on understanding ion transport through mixed GBs in YSZ, despite their dominating presence in the samples. Herein, we present an experimental and theoretical study to identify the mixed GB distribution and analyse their oxygen-ion conductivity. First, polycrystalline YSZ samples were fabricated in the form of sintered ceramic pellets. Then, we use TEM to identify the type of GBs present in the sample. Finally, the structure and transport properties of the mixed GB at several Y_2O_3 concentrations and temperatures were modelled computationally, and the results were compared with the high symmetry $\Sigma5$ ($\Sigma5 = (310)/[001]$) GB, $\Sigma11$ ($\Sigma = 11(311)/[110]$), $\Sigma13$ ($\Sigma = 13(510)/[001]$), another mixed GB formed by (20−1) and (100) planes and the single crystal models. Finally, the underlying reason for the obtained conductivities of different GB samples was discussed by coordination number analysis.

2 Methodology

2.1 Sample preparation

Commercial 8 mol% YSZ powder—TZ-8Y, was purchased from Tosoh (Japan). The powder was compacted to a disc-shaped pellet by uniaxial hydraulic pressing with a pressure of 19.68 MPa and subsequently *via* cold isostatic pressing at a pressure of 250 MPa for 10 min. The diameter of the pellet die was ~18 mm. The green pellets were then sintered at 1400 °C for 5 h.

2.2 Scanning electron microscope (SEM) characterization

2D Electron backscatter diffraction (EBSD) maps were acquired on an SEM using TSL OIM backscatter diffraction camera. An accelerating voltage of the electron beam was set to 15 kV. Orientation maps were acquired from 100 by 100 μm regions with square grid pattern and 150 nm step size.

2.3 Transmission electron microscopy characterization

TEM thin foil samples were prepared by ion milling after slicing, and mechanical thinning of the YSZ sintered material. The GB was observed using Titan ETEM, FEI, with aberration collection operated at an accelerating voltage of 300 kV.

2.4 Simulation details

LAMMPS (Large-scale Atomic/Molecular Massively Parallel Simulator),[31] an MD simulations package, is used to generate the mixed GB's atomic model *via* amorphization and recrystallization (A&R) strategy.[32,33] The interatomic potentials used for MD calculations are described by a rigid-ion Buckingham type potential. The short-range Buckingham potential was combined with a long-range coulombic term to model ionic interactions properly.

Thus, the potential for the interaction between two ions *i* and *j* at a distance *r* is defined by the following equation:

$$U_{ij}(r) = A_{ij}e^{\frac{-r}{\rho_{ij}}} - \frac{C_{ij}}{r_{ij}} + \frac{q_i q_j}{4\pi\varepsilon_0 r_{ij}} \tag{1}$$

where the parameters A_{ij}, ρ_{ij}, and C_{ij} (Table S1†) are taken from the previous studies of Grimes *et al.*[34,35] This potential was parameterized regarding experimental data, and it was shown to successfully predict lattice parameters, defect formation and activation energies, and bulk diffusion.[36–38] The chosen potential reproduces the cubic phase of YSZ rather well as reported in the literature.[13,15,39–41] However, it is not very successful in reproducing neither tetragonal or monoclinic phases.[40] The system is considered completely ionic where the ionic charges for Zr, Y, and O ions are taken as full ones, +4, +3, and −2, respectively. The Ewald method[42] was used to compute the long-range coulombic interaction component of the eqn (1), and the short-range part of the potential is calculated with a cutoff distance of 11 Å. For all MD simulations, an orthogonal simulation box is used with a velocity-Verlet integration scheme and a time step of 1 fs.[43]

The oxygen-ions diffusion was determined by the mean squared displacement, MSD(*t*), given by:

$$\text{MSD}(t) = \frac{1}{N}\sum_{n=1}^{N}\left[r_n(t+t_0) - r_n(t_0)\right]^2 \tag{2}$$

where $r_n(t+t_0)$ and $r_n(t_0)$ are the position of the n^{th} ion at time $t + t_0$ and t_0, respectively. N is the number of ions that are diffusing (only oxygen atoms in our case). MSD(*t*) is related to the self-diffusion coefficient *via* Einstein relation:

$$D = \lim_{t\to\infty}\frac{\text{MSD}(t)}{6t} \tag{3}$$

where *D* is the self-diffusion coefficient, and *t* is the time of diffusion.

3 Results and discussion

3.1 Statistical distribution of GBs in YSZ sample

The XRD pattern (Fig. S1†) confirms that the 8YSZ bulk part is polycrystalline, the peaks are indexed to the YSZ crystal planes, indicating cubic phase with low or non-existent impurities. The lattice parameter calculated from the XRD pattern is 0.514 nm, which is in good agreement with our computationally obtained

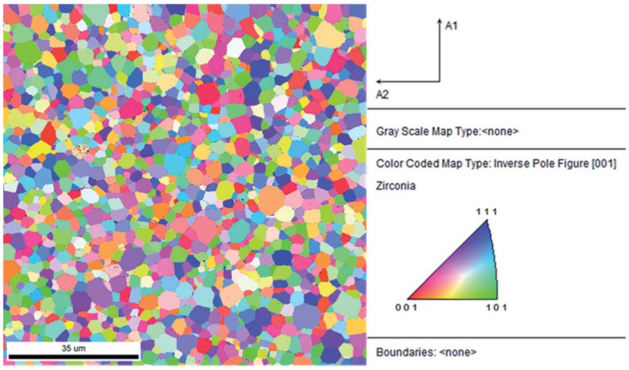

Fig. 1 2D inverse pole figure (IPF) EBSD map of YSZ polycrystalline pellet. The reference triangle is placed at the right.

value of 0.514 nm for 8YSZ.This lattice parameter also agrees closely with the ones reported in literature.[13,17,44]

In order to identify the prominent GBs in the prepared sample, first, we conducted an EBSD-SEM analysis. Fig. 1 represents the statistical overview of the grains in the sample coupled with the grain map illustrating the individual grains. The grains were identified by defining a critical misorientation angle within the polycrystalline YSZ pellet.

The 'misorientation angle' is the most common and valuable descriptor used to provide the rotation angle between the grain orientation planes. For our sample, the distribution of misorientation angles of GBs is represented in Fig. 2. It was found that most of the misorientation angles at GBs were larger than 15°. Therefore, most of the GBs present in our pellet were high-angle GBs. Two local maxima were identified in the misorientation angle distribution of our sample: first in the range of 42–47°, and the second in the range of 47–52°. In other words, most of the GBs in the sample have a misorientation angle between 42–52°, and, therefore, their behaviour will be critical in determining the overall transport properties of the samples.

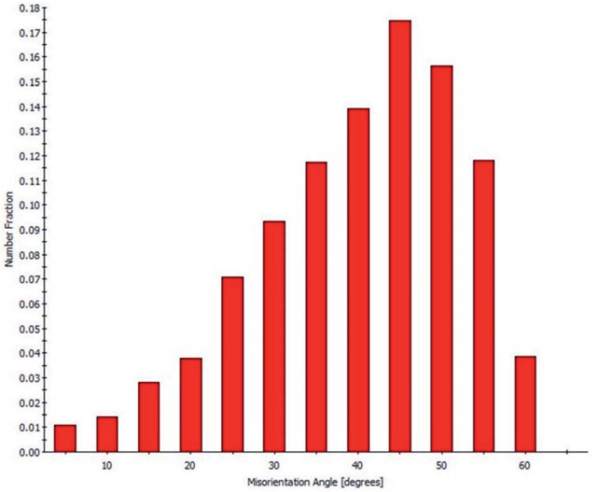

Fig. 2 Misorientation angle distributions in the prepared YSZ sample.

Furthermore, the EBSD-SEM analysis allow to plot the individual CSL GBs fraction contained in the pellet according to the overall GB population (Fig. S2†). The CSL GBs fraction is 17% of the sample, with the largest fraction being type Σ3 followed by Σ5, Σ9 and Σ11 GBs. The fraction of CSL GBs agrees with the value previously reported by Vonlanthen and Grobety (17.8%).[45]

3.2 Computational model preparation of mixed GB

Dopant segregation and oxygen diffusion has been widely studied for fluorite based materials. Previous studies confirmed that defect segregation towards GBs in different polycrystalline doped-oxides is thermodynamically favoured process, leading to degradation of the material and a reduction in oxygen conductivity.[15,18,46–48] However, different materials and different GB structures have different behaviour as suggested by several studies.[18,49–51] In order to investigate the effect of mixed GBs on oxygen-ion transport in the YSZ sample, we chose to model the mixed GB formed with (−511) and (21−1) surfaces and misorientation angle of 52°. This GB was identified by TEM (as illustrated in Fig. 3(a)) and selected as an example among several other similar GBs observed in the sample. We used the A&R technique to design the realistic model of the mixed GB, as shown in Fig. 3(b). In Fig. 3, the original model was visually repeated along the *Y*-axis and the oxygen atoms were removed for better comparison with the TEM image.

To prepare the mixed GB model, we used the starting periodic supercell structure having low built-in strain and a reasonable number of atoms. The initial structure was achieved by VNL (Virtual NanoLab),[52] which allows an efficient and systematic search for common supercells between two crystalline surfaces by varying the interface strain and the rotation between them. This search resulted in a model having both surfaces aligned parallel at an optimized distance of about 7 Å, with zero angles of orientation, a total strain of 0.98% between them, and the lowest possible number of atoms (648). This model was then repeated ten times along the *X*-axis and two times along the *Y*-axis to obtain the desired initial model having thick enough grains with 6240 atoms each (2080 Zr^{4+} and 4160 O^{2-}), so the effect of yttrium substitutional defects ($Y_{Zr'}$) can be adequately observed. In total, both surfaces were constructed with 54 layers along *Z* (the grain boundary axis) to maintain the same initial thickness for both grains. In order to obtain the 8% Y_2O_3 doped ZrO_2 models, Zr^{4+} atoms were substituted randomly by Y^{3+} in the structure, and for every two atoms substituted, one V_O was created. It should be noted that the TEM image showed a deviation of 1.7° concerning the grain orientation (21−1) with respect to the GB plane. However, no deviation between the two surfaces was considered in our starting model. They were allowed to rotate freely during the A&R process.

To conduct the A&R process, we used the NPT (constant number (*N*), pressure (*P*), and temperature (*T*)) ensemble for amorphization as well as recrystallization steps. For amorphization, the optimum melting temperature for our model was found at 5200 K for 690 ps (Fig. 4(b)). Experimental samples are synthesized with short annealing times which leads to the kinetically favourable atomic arrangement, with an appropriate

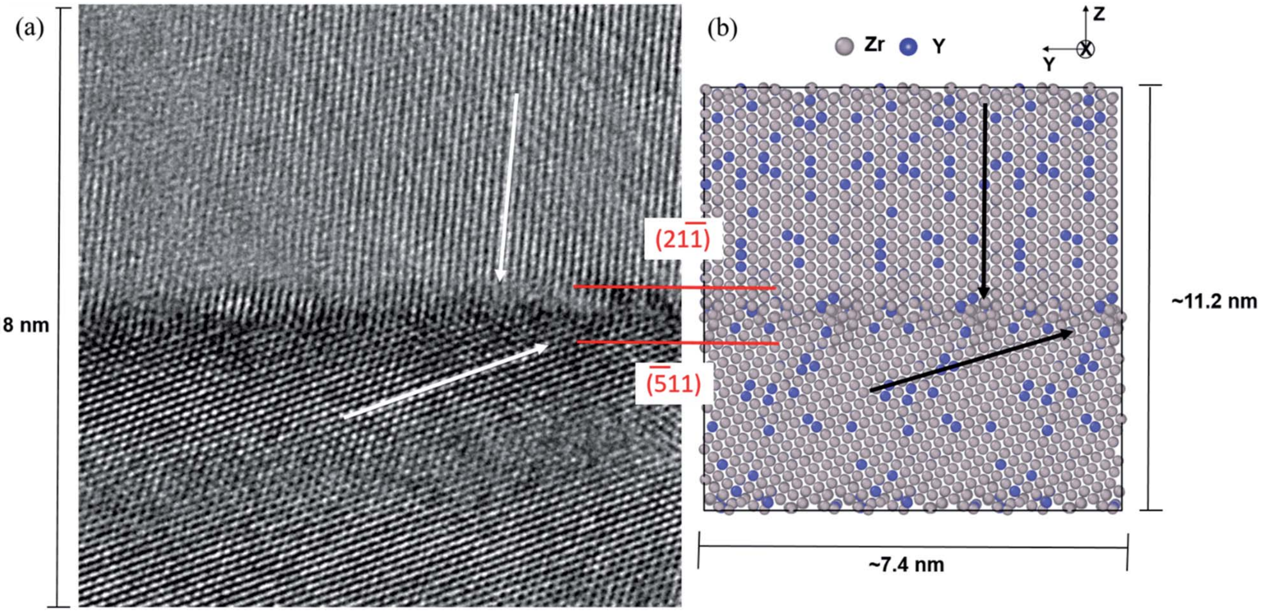

Fig. 3 (a) The TEM image of a mixed GB formed by (−511) and (21−1) orientated grains, with a misorientation angle of 52° and (b) the computational model representing the same mixed GB, prepared by amorphization and recrystallization method.

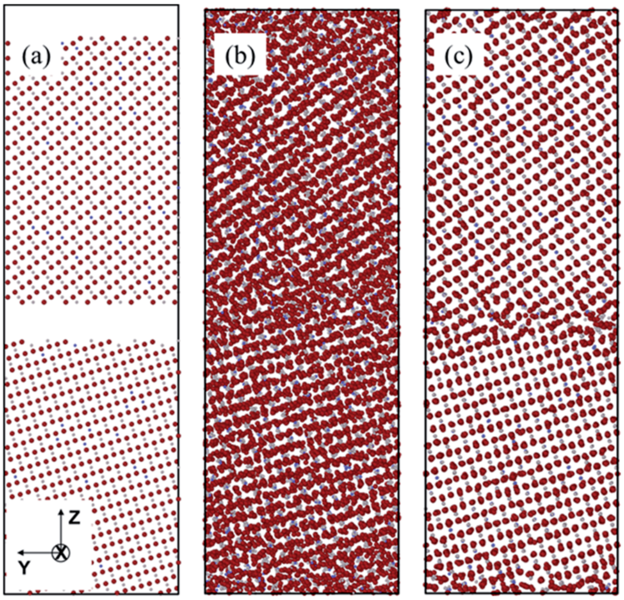

Fig. 4 (a) Initial structure (with 7 Å void between the two grain surfaces, (21−1) at the top and (−511) at the bottom), (b) amorphized structure, and (c) recrystallized structure of YSZ grain boundary system. O^{2-}, Zr^{4+} and Y^{3+} are represented by red, blue and grey spheres, respectively.

randomized dopant distribution. To simulate this process *via* molecular dynamics, we require higher operating temperature since the simulation time will be a very small fraction of the experimental annealing time.[53–56] Therefore, the two surfaces have been put close together and then temperature was raised until we achieve complete amorphization of the structure without losing the short range order of each grain. The RDF was checked after every few steps to make sure our sample is getting to the amorphous state. When the system is relaxed, the initial gap between the two grains disappears completely and during the heating process, it starts to form the highly disordered GB with comparatively less disordered grains. Further, since oxygen has lower atomic mass (~16 u) as compared to cations (Y (~88.90 u) or Zr (~91.22 u)), we see more disorder in O atoms compared to cations as illustrated by RDF of O–O, Zr–Y and Zr–Zr (Fig. 5). Beyond this temperature (*i.e.* 5200 K) our system makes solid solution and could not be recrystallized. It's important to mention that according to Dillon and Harmer's GB complexion theory, different sintering or simulation conditions during the model preparation may lead to different GB phases or complexions with different properties and behaviour.[57–59] Therefore, it is possible that we might have obtained the microstructural features in our GB models that are not present in the experimental samples. After randomization, recrystallization was induced by reducing the system's temperature from 5200 K to 20 K in 500 ps using an NPT ensemble, which recrystallized the system (Fig. 4(c)). After recrystallization, the system was equilibrated for 100 ps, followed by final potential energy minimization in order to remove any internal stress in the material caused during the recrystallization.[60] Minimization is performed using a built-in function in LAMMPS that iteratively adjusts the atomic coordinates to minimize the potential energy using a conjugate gradient optimization algorithm. For a more straightforward 3D interpretation of the arrays of atoms, cations' radius was reduced visually in Fig. 4.

Further, 4YSZ, 11YSZ, and 14YSZ mixed GB models were prepared to investigate the effect of Y-doping. The mixed GB models were also compared with the high symmetry Σ5 GB. All the models were prepared *via* the same A&R strategy. The final

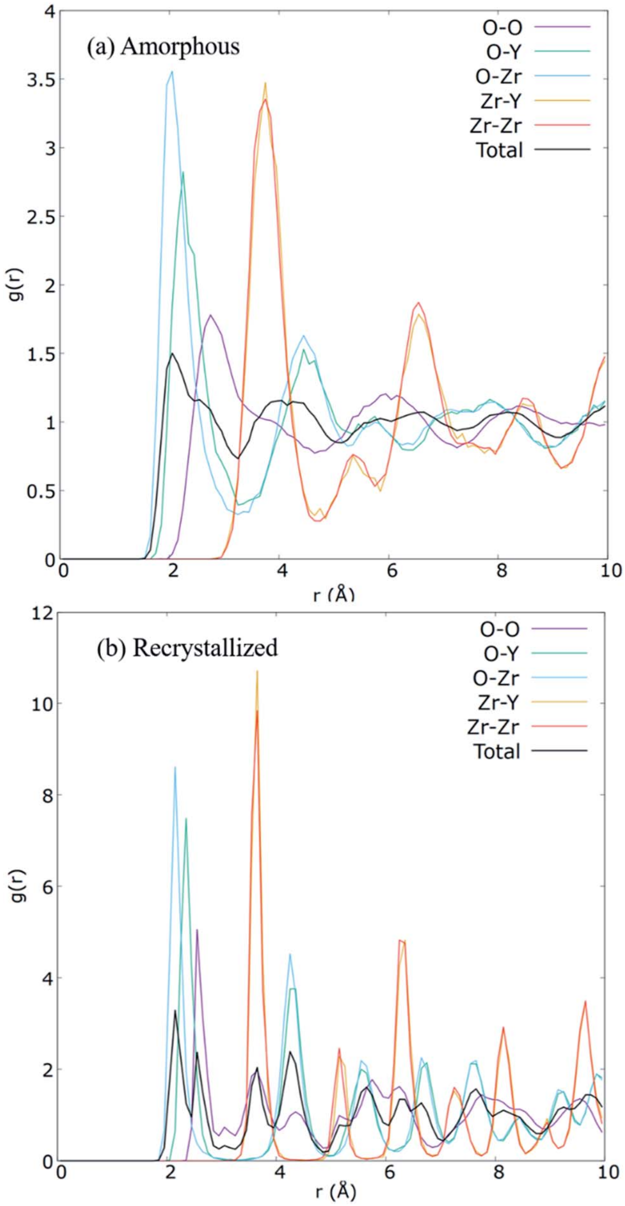

Fig. 5 Calculated partial radial distribution functions for each ionic pairs in the (a) amorphized, and (b) the recrystallized 8YSZ GB systems.

structures of 4YSZ, 11YSZ, 14YSZ, and Σ5 are represented by Fig. S3 in ESI .†

3.3 Structural properties of mixed GB

The A&R process was verified *via* partial radial distribution function (RDF), $g(r)$. RDF outlines the average spatial organization of atoms in the cell lattice. Partial RDFs are distinct between ionic pairs. Consequently, Fig. 5 plot the contrasting RDFs of the amorphous and recrystallized YSZ GB models. For the recrystallized structure (Fig. 5(b)), well-defined pronounced peaks are observed. These peaks' location corresponds to the distance of the average closest neighbouring atoms between pairs, a sign of long-range order preservation. Hence, when ZrO_2 is doped with Y_2O_3, it is expected that the creation of V_O distorts the peaks for the O–O pair, as also observed for our prepared sample. After A&R, the local position of O^{2-} surrounding V_O changes toward or away from it,[13,61] resulting in broader peaks for the O–O pair (Fig. 5(b)). Further, at 20 K the average closest-neighbour O–O, O–Zr, O–Y, and Zr–Y distances are estimated as ~2.55, 2.15, 2.35, and 3.65 Å, respectively, which agree with the experimental and computational crystallographic data reported in the literature.[62,63]

In contrast to the RDF of the recrystallized model, RDF for the amorphous model (Fig. 5(a)) shows a left shift in the short-range peaks of O–Zr, and O–Y at 2.05, and 2.25 Å, respectively, and a right shift in the peaks of O–O and Zr–Y at 2.75 and 3.75 Å, respectively. Further total RDF after 4 Å as well as partial RDF of O–O, O–Zr, O–Y showed no significant long range structure, as reported in other theoretical studies of amorphous YSZ.[63–65] However, in this work we did not achieve the solid solution as expected for amorphous structures, instead we have a short range disordered structure after amorphization step, needed to recrystallize the system.[64,65] The broader peaks observed along r (Å) for the amorphous structure and the sharp peaks observed for the recrystallized structure clearly show the success of the A&R process.

Furthermore, it was found that the system's volume substantially increases during the heating process, resulting in the 38.3 × 38.7 × 116.9 Å cell dimensions and decreases during the cooling process, resulting in the 36.5 × 36.9 × 112.1 Å cell dimensions for the recrystallized structure. In addition, an excess volume of 1.93% was calculated in comparison with the single-crystal model. The observed increase in volume is due to the 0.98% tensile strain on both grains in the initial model.

The A&R process enabled both the grains to grow a realistic GB between them. It should be noted that Y^{3+} substitutional defects and oxygen vacancies (V_O) are introduced before the A&R process so that the GB model can achieve a low energy configuration while inducing possible segregation of Y^{3+} and V_O. In this work, following the previous methodology,[66] the use of the NPT ensemble successfully allowed our system to design GB properly without being influenced by the initial void chosen between the grains contrary to the simulations conducted with the NVE ensemble.[67] This was confirmed by performing A&R on a starting supercell having shorter (5 Å) and larger (10 Å) void between the two grains. All the starting supercells with voids of 5, 7, and 10 Å resulted in similar final structures (For more details, refer to Fig. S4†).

To further understand the mixed GB structure, we calculated the O, Y and Zr ion densities in the prepared model. Fig. 6 represents the one-dimensional (1D) ionic count of O^{2-}, Zr^{4+}, and Y^{3+} along the z-axis (perpendicular to the GB plane) of 8YSZ. The disorder at the GB core corresponds to an approximate thickness of 1.2 nm, five atomic layers, represented by dotted lines in Fig. 6. It also reveals that the thickness of left (−511) and right (21−1) grains are 4.7 nm and 5.3 nm approximately, resulting in the mixed GB periodic model of 11.2 nm. Several local minimum peaks exist in the 1.2 nm GB core, indicating the GB core's low ion density. Further, O^{2-} density is minimum at the GB core while its maxima can be seen at the ends of the GB core, denoted as 'edges' of the GB core (represented by the

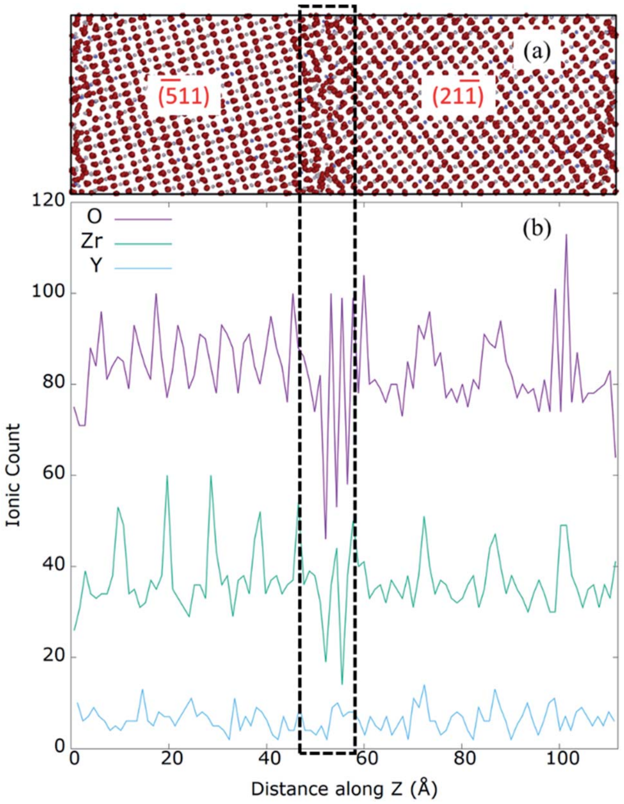

Fig. 6 (a) 8YSZ GB system. O^{2-}, Zr^{4+} and Y^{3+} are represented by red, blue and grey spheres, respectively. (b) Calculated ionic count as a function of distance perpendicular to the GB core. The dotted box in (a) and (b) represent the GB core.

dashed black line). The average anion/cation stoichiometry for 8YSZ is 1.93; at the GB core, the measured stoichiometry is 1.88, proving the deficiency of O^{2-} and consequently, segregation of V$_O$ at the GB core. These results agree with previous works,[19,68] and are likely responsible for the predicted space-charge regions due to V$_O$ and possibly Y^{3+} segregation at the GB core and their depletion in the adjacent bulk regions.[69,70]

3.4 Yttrium distribution in mixed *vs.* symmetric GBs

First, we investigated Y^{3+}, O^{2-} and Zr^{4+} concentrations in our prepared mixed GB model. As shown in Fig. 6, the Zr^{4+} and O^{2-} ion density significantly varied at grain interior and GB core. In contrast, our mixed GB model showed no drastic change in Y^{3+} concentration along the *z*-axis between GB core and grain regions. The Fig. S5† shows the normalized ionic count with respect the total number of ions of each specie. There, a higher fraction of Y^{3+} can be observed at the GB core and its surroundings, especially if it's compared with the O^{2-} and Zr^{4+} fractions. However, taking into account the distribution of Y^{3+} through the whole model, it cannot be considered that the segregated quantity of Y^{3+} is as significant as has been reported previously by other studies in the literature.[7,14,21,71,72] This apparent discrepancy can be explained considering that our MD production run is only conducted for 500 ps, which is very small to see any significant Y^{3+} segregation. Practically, Y^{3+} segregation at GB is a time-dependent process and happens over long operation time of SOFCs.[15,18,20]

Shibata *et al.* experimentally investigate thoroughly the effect of Y^{3+} segregation and its effect on blocking oxygen diffusion on Σ3 and Σ5 bicrystal.[7,51,73–75] Gonzalez-Romero *et al.* reported several MD studies where they had added extra energy to Y^{3+} cations to overcome the difficulties of classical methods to yield segregation naturally by itself.[15,18] However, it should be mentioned that irrespective of the technique used, previous MD studies suggest that Y^{3+} segregation does not seem to affect the oxygen-ion conductivity at the GB significantly.[11,15,17,18,20] However, it has a major impact on the overall conductivity since V$_O$ tends to be the second nearest neighbours of Y^{3+} cations.[13,14] Furthermore, it is unclear how Y^{3+} distribution in the samples is affected by grain orientations. As mentioned previously, 500 ps is not enough to see Y^{3+} segregation, but by analysing the ionic density of Y^{3+} before and after the A&R process, for both mixed GB and the high symmetry Σ5 GB (Fig. 7), we can understand if grain orientation influences the distribution of Y^{3+} or not. In both GBs, Y^{3+} moves away from the GB core to the edge of the GB core after relaxation. In the mixed GB, along with the two new peaks at the edge of the GB core (shown by black arrows in Fig. 7(a)), Y^{3+} gets accumulated in the (21−1) grain interior (shown by red arrows in Fig. 7(a)). Such behaviour was not found for Σ5, where fewer structural differences exist between the two grains forming the GB in agreement with the literature.[13] The predominant effect seen in the Σ5 GB is the

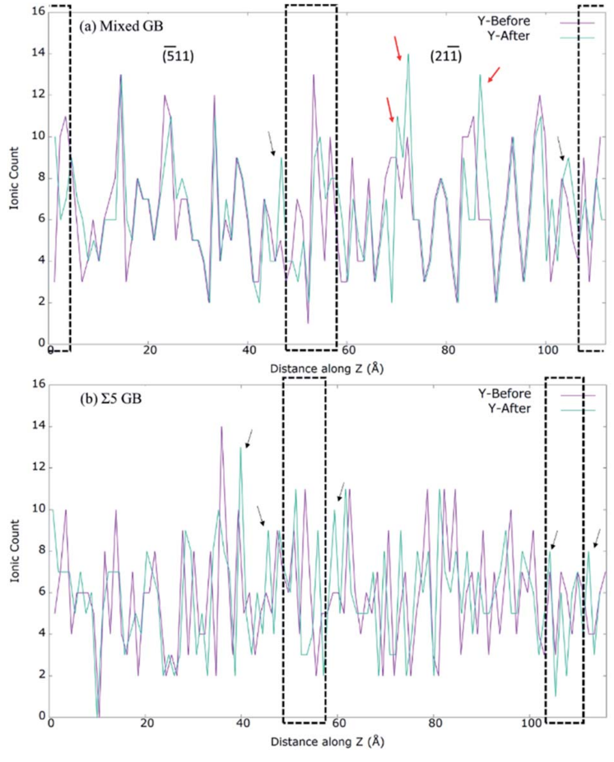

Fig. 7 Calculated Y-ion count along *z* direction for (a) 8YSZ mixed GB system. (b) 8YSZ Σ5 GB system. The dotted box in (a) and (b) represent the GB cores.

segregation of Y^{3+} ions at the edge of the GB core (indicated by the black arrows in Fig. 7(b)).

To confirm if this behaviour is characteristic of mixed GBs, three more 8YSZ GBs were modelled: (a) another mixed GB observed by TEM in the sample and formed by planes (20−1) and (100) with a misorientation angle of 26.6° (Fig. S6†); (b) Σ13 (510)/[001] GB; and Σ11 (311)/[110] GB. The recrystallized structures are shown in Fig. S7.† The yttria content of the mixed GB within the (100) and (20−1) grains didn't change during the A&R. In (100) grain the content of Y^{3+} seems well ordered and uniformly distributed, and only small signs of segregation can be observed close to the GB edges (Fig. S8†). On the other hand, Σ13 presents a more significant rearrangement of Y^{3+}, with yttria segregation close to the GB core as well as inside the bulk. Lastly, Σ11 the most symmetric GB showed accumulation of Y^{3+} in one of the grains and towards the GB. Clearly, this analysis shows that segregation of Y^{3+} is dependent on grain orientation.

3.5 Oxygen diffusion in mixed GB at different temperatures

The oxygen self-diffusion (D_o) was analysed through the mixed GB at various operating temperatures. First, to better understand the influence of the GB with respect to bulk, the Mean Squared Displacement (MSD) was calculated from the total squared displacement of oxygen-ions in all three (X, Y, Z) directions *i.e.* ($dx*dx + dy*dy + dz*dz$), where dx, dy, dz corresponds to change in position of the ion in X, Y, and Z directions, respectively. Considering the Z-axis as a reference, three regions of 2 nm each were selected for representing core GB, (−511) grain, and (21−1) grain. The grain regions were selected as farther as possible from the GB core, as represented by red boxes in Fig. 8. The left part of the figure shows the MSD results for all three regions at 2300 K. Here, the real blocking effect of the GB in the oxygen-ion conductivity can be noticed. Calculating the oxygen self-diffusion coefficient (D_o) from the total MSD allows us to compare the differences in oxygen migration between regions; the results are summarized in Table 1. The GB core shows a D_o, 4.85×10^{-10} m^2 s^{-1}, much lower than both grains, as expected. However, to our surprise, we found a significant difference in diffusivity between the two grains. The (21−1) grain ($D_o = 1.24 \times 10^{-9}$ m^2 s^{-1}) showed diffusivity almost double than (−511) grain ($D_o = 8.69 \times 10^{-10}$ m^2 s^{-1}). Interestingly this gap between the diffusivity of both grains indicates that during the formation of GBs, the grain orientation toward the GB plane plays an important role in oxygen diffusion inside the grain. Such effect is not noticeable when modelling highly symmetric GBs.[13,15,17,18,20] To verify these findings, the MSD at 2300 K was calculated (Fig. S9†) for the oxygen atoms contained in two single-crystal structures modelled with the orientation planes of the mixed GB structure: (21−1) and (−511). The almost identical MSD results for (2−11) and (−511) single crystals confirm that GB is critical in determining oxygen diffusion inside the constituent grains.

Table 1 Calculated oxygen self-diffusion coefficient (D_o) for mixed GB systems at 2300 K in m^2 s^{-1}

Model	Total	GB core	Grain 1 (−511)	Grain 2 (21−1)
4YSZ	9.39×10^{-10}	3.35×10^{-10}	8.21×10^{-10}	1.09×10^{-9}
8YSZ	1.07×10^{-9}	4.85×10^{-10}	8.69×10^{-10}	1.24×10^{-9}
11YSZ	1.05×10^{-9}	6.10×10^{-10}	9.04×10^{-10}	1.14×10^{-9}
14YSZ	9.06×10^{-10}	3.85×10^{-10}	6.44×10^{-10}	9.17×10^{-10}

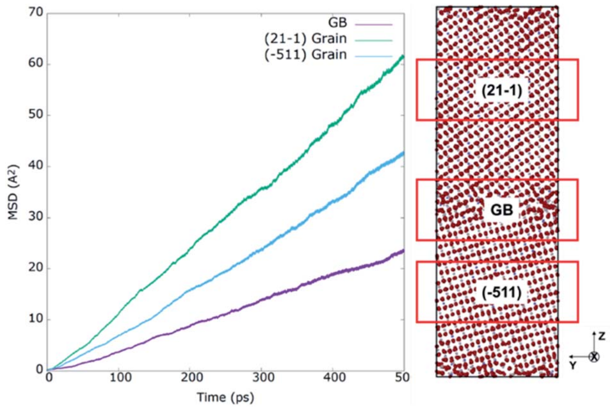

Fig. 8 Mean square displacements at 2300 K for regions of 20 Å along z axis containing the GB core, (21−1) and (−511) grain interior regions of 8YSZ mixed GB system.

To better understand the effect of grain orientation on the overall performance of the mixed GB system, further investigations of the oxygen self-diffusion were carried out. Models with 4%, 11%, and 14% Y_2O_3 dopant concentrations were prepared using the same parameters and technique described above and were investigated under a range of temperatures between 700–2300 K. Fig. 9 plots the Arrhenius relationship between Ln of D_o and the inverse of temperature. At the GB core (Fig. 9a), 8 and 11YSZ seem to have the optimum Y_2O_3 content, enabling best ionic diffusivity for operating temperatures between 1000-1200 K. Above 1200 K, the highest D_o for the GB core is found for 11YSZ. At lower temperatures (<1000 K), empirical potentials have difficulties describing oxygen migration, which is why 4YSZ shows the highest D_o at 700 K. The same effect is observed at the grain interior (Fig. 9b and c) where the maximum diffusivity is observed for 4YSZ for the range of temperatures between 700 K and 1500 K. In this low-temperature range, MD calculations do not accurately represent the energy given to the oxygen-ions to diffuse through the vacancies in a short production time (0.5 ns). Consequently, the activation energies (E_{Act}), represented in Fig. 9, have been calculated through the Arrhenius plot considering only values from 1200 K to 2300 K. The GB core presents higher E_{Act} than grains as expected. Within the GB core region, the values don't vary significantly with the increasing amount of yttria. On the other hand, we can see a larger contrast between different Y_2O_3 within the grains regions, specially between 4YSZ and 8YSZ. However, this difference seems to be reaching its maximum around 14YSZ, in agreement with previous studies.[13,15,63]

Furthermore, even though it is well known that experimentally, 8YSZ presents the highest oxygen diffusivity for a wide range of temperatures, in MD, the highest diffusivity under 2000 K is often found for Y_2O_3 content below 8 mol%.[17,63,76–78] In

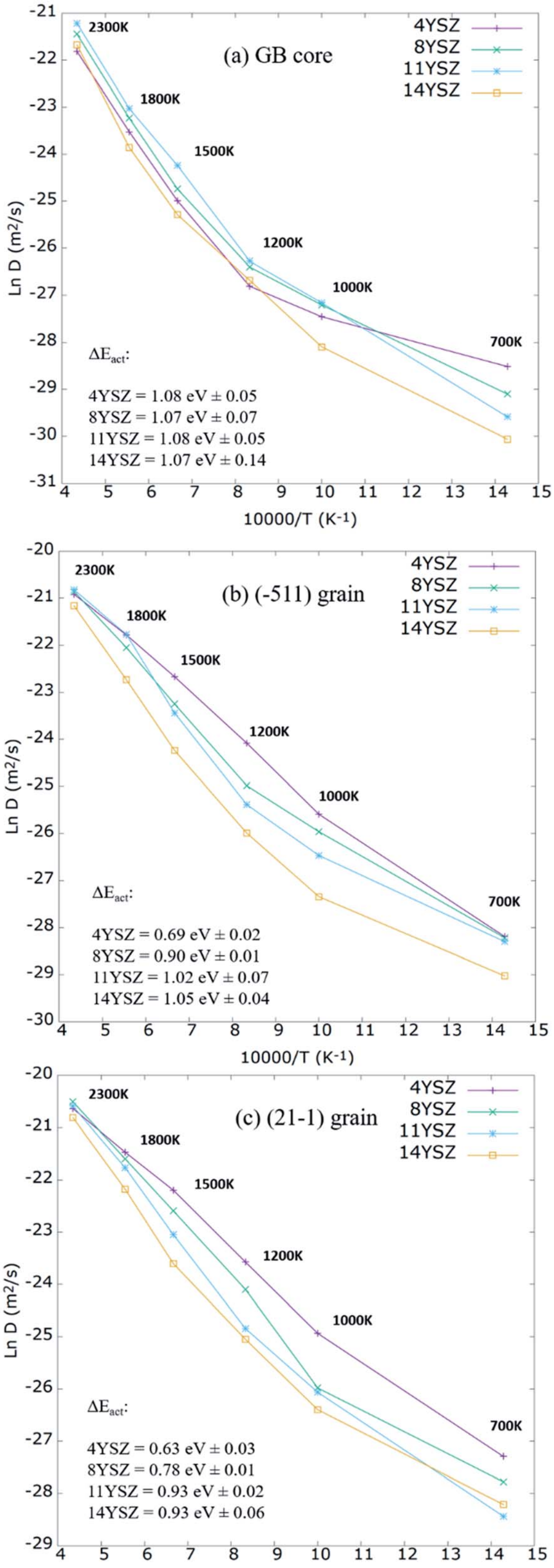

Fig. 9 Arrhenius plot of oxygen self-diffusion with respect to the temperature ranging from 700 to 2300 K of doping concentrations between 4–14 mol% for (a) GB core, (b) (−511) grain interior and, (c) (21−1) grain interior.

contrast, at higher temperatures (1800−2300 K), 8 and 11 mol% are the optimum concentrations for O^{2-} mobility. Furthermore, it should be noted that according to our calculations, oxygen diffusion should be more impeded for concentrations ≥ 14 mol% at temperatures between 700–2300 K.

These results agree with the optimum concentration reported for YSZ single crystal,[17,63,79] symmetric GB,[9] and amorphous phase.[63] Lastly, it should be noted that the diffusivity of both grains follows the same trend for different Y_2O_3 doping concentrations and temperatures despite their structural differences.

3.6 Conductivity of mixed GB *vs.* Σ5 *vs.* SC

To identify the role of grain orientation on O^{2-} ion diffusion, next we investigated D_o in Σ5 GB and single crystal (SC) and compared it with that of mixed GB at 2300 K. The reason for choosing this temperature instead of the average operating temperature of SOFC (∼1000−1200 K) is the difficulties reported previously to correctly describe the diffusion coefficient at temperatures below 2000 K[17,63,76–78] MSD calculations were performed for the prepared 4−14 mol% YSZ mixed and Σ5 GBs and compared with the SC system. Fig. 10 shows the calculated D_o for the three complete systems as a function of the Y_2O_3 content at 2300 K. The optimum Y_2O_3 content was found for 8 mol% for all three systems. However, D_o is quite different between GBs and SC systems. The low D_o of GB systems indicates how the presence of GBs obstructs the oxygen-ion migration. Further, this effect is higher for the mixed GB than for Σ5. In SC, the optimum concentration is clearly 8YSZ. However, in GB-containing systems, the optimum concentration may be higher than 8YSZ, as the difference between 8 and 11YSZ is not

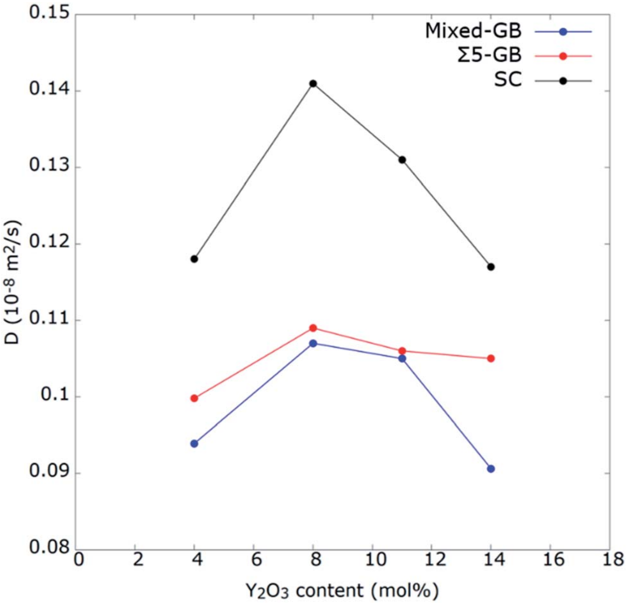

Fig. 10 Self-diffusion coefficients of oxygen ions as a function of doping concentration for YSZ mixed GB system, Σ5 GB, and SC at 2300 K.

Table 2 Calculated oxygen self-diffusion coefficient (D_o) for 8YSZ mixed and Σ5 GB systems and SC at 2300 K in $m^2 s^{-1}$

Model	Total	GB core	Bottom grain	Top grain
Mx GB (−511) (21−1)	1.07×10^{-9}	4.85×10^{-10}	8.69×10^{-10}	1.24×10^{-9}
Mx GB (20−1) (100)	1.19×10^{-9}	4.60×10^{-10}	7.23×10^{-10}	1.51×10^{-9}
Σ5 (310) GB	1.09×10^{-9}	5.21×10^{-10}	1.14×10^{-9}	1.14×10^{-9}
Σ11 (311) GB	1.20×10^{-9}	7.93×10^{-10}	1.17×10^{-9}	1.17×10^{-9}
Σ13 (510) GB	1.07×10^{-9}	5.12×10^{-10}	1.09×10^{-9}	1.09×10^{-9}
SC	1.41×10^{-9}	—	—	—

as pronounced as in SC. These results are in good agreement with the reported literature for Σ5 and SC.[13,20,63]

Furthermore, the presence of GB causes a decrease of the interior diffusion in grain as compared to that in SC model that show a D_o of about 1.41×10^{-9} $m^2 s^{-1}$ at 2300 K (Table 2). It can be explained as an aftereffect caused by the low diffusivity in the GB core that extends over the grains, as explained by Huang *et al.*[17] On the other hand, it also might be caused by the segregation of Y^{3+} toward the GB's core as suggested by Gonzalez-Romero *et al.*,[15] who induced Y^{3+} segregation externally. Nonetheless, they noticed that the effect did not appear at the GB core, where oxygen-ions rearranged themselves during the diffusion. Instead, the effect of Y^{3+} segregation appeared in the grain interior, where the number of oxygen-ions as second neighbours for $Y_{Zr'}$ defects dropped drastically. In this work, as explained earlier, segregation of Y^{3+} was found to be favoured by (−511) grain which also showed low D_o. In contrast, (21−1) grain showed diffusivity close to that of SC. Interestingly this behaviour was also observed for the (20−1) (100) mixed GB, where the oxygen self-diffusion in grain (100) was almost twice as high as in grain (20−1). This is due to the reason that (100) grain has well distributed V_o along the *Z* direction (Fig. S8†), allowing an easy oxygen ion diffusion. On the other hand, for the CSL GB systems, Y^{3+} segregates towards the GBs core due to the symmetry of both grains,[28] and interestingly our calculation shows that the oxygen self-diffusion of their grain interior are lower than that calculated for the (21−1) or (100) grains (Table 2). This demonstrates that grain orientations have a massive impact on the oxygen conductivity of the system, and all GBs should not be treated the same. From these results, we can conclude that grain orientations favouring Y^{3+} segregation will present lower D_o at the grain-interior region close to the GB than those preventing it. That being said, this effect is probably negligible in polycrystalline samples with grain sizes equal of greater than micrometre scale because the bulk part affected by the segregation of Y^{3+} would be a small percentage of the whole grain interior size. However, it should be noted that the creation of space-charge regions takes place inside the grains, close to

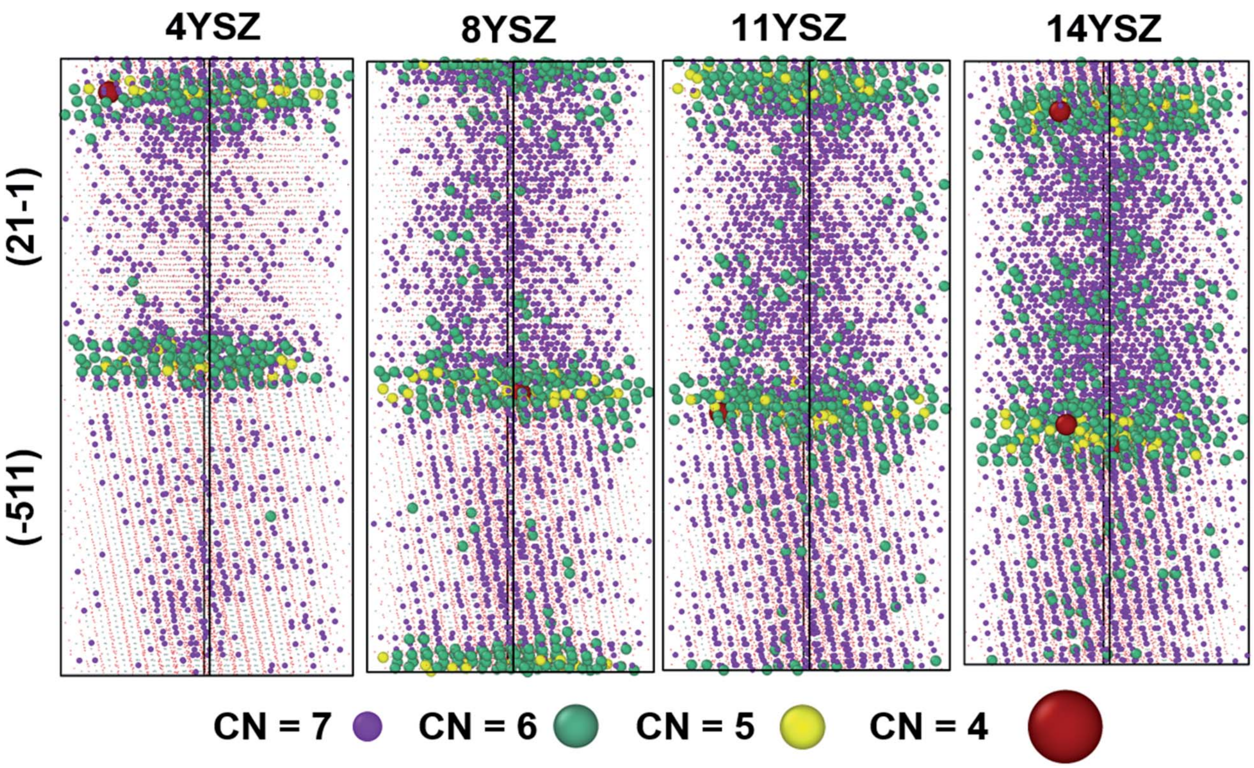

Fig. 11 Cation distribution inside the YSZ GB system in terms of their coordination number.

the GBs, and they extend several nanometres towards the bulk.[47,80,81] Therefore, the space-charge regions would seriously impact YSZ samples having the nanoscale grain sizes, decreasing their conductivity significantly.[69,81]

3.7 Coordination number analysis in mixed GB

The oxygen-ion diffusion is different for different regions of the prepared mixed GB sample. Table 2 summarizes this difference in the oxygen self-diffusion coefficient for every region of the GB model at 2300 K. It is crucial to understand the origin of this difference in diffusivities to improve the overall conductivity of YSZ samples *via* GB engineering. Therefore, we further analysed the oxygen vacancies distribution *via* cation coordination number analysis. Fig. 11 represents the distribution of cations with coordination number < 8 for the first nearest-neighbour shell, therefore the cutoff radius was set at 3 Å. The average coordination number for cations decrease from 7.6 for 4YSZ to 7.14 for 14YSZ. The decrease in coordination is caused by increasing yttria's doping concentration, increasing the number of oxygen vacancies.

It should be noted that the 7-coordinated cations are more uniformly distributed for grain (21−1) than for (−511) orientation for all the samples with different yttria doping content. In addition, at the edge of grain (21−1), they are more uniformly distributed than in (−511) grain. For each composition, the average coordination is lower at GB than at grain, indicating that cations at GB core attract oxygen vacancies as also reported by González-Romero *et al.*[13] However, in our system, the accumulation of Y^{3+} inside (21−1) grain allows a uniform distribution of V_O along the grain interior favouring the easy oxygen-ion diffusion in this region. On the other hand, the grain orientation (−511) seems to have many areas with only 8-coordinated cations (plotted as dots in the figure for more straightforward visualization). Consequently, because of the lack of V_O, oxygen-ion migration become harder in these areas. Furthermore, Table S2† shows the percentage of cations with different coordination at the different cell regions for each doping concentration. As expected, most of the low coordinated cations (6 and below) are found at the GB cores due to the accumulation of V_O and the lack of crystallinity.

Furthermore, the two grains behave differently. The 7-coordinated cations predominate in (21−1) grain irrespective of the doping concentration in the sample. 8YSZ seems to have the best distribution of oxygen vacancies, facilitating the oxygen diffusion. Higher concentrations of Y_2O_3 lead to a higher number of Y_{Zr}–Y_{Zr} defects clustering, increasing the probabilities of having trapped oxygen vacancies, hindering the oxygen mobility, as observed in the 14YSZ system.[18,82,83] On the other hand, 11YSZ shows the highest 7-coordinated cation concentration and consequently the lowest oxygen vacancy clustering, which leads to the highest D_o at the GB core among all the samples.

4 Conclusions

GBs with a misorientation angle between 47° and 52° are found to be the most common GBs in our YSZ sintered ceramic pellets. A mixed GB with 52° angle was identified among others using TEM and analysed in this work *via* classical MD. First, a realistic model of the mixed GB was prepared *via* the A&R technique. Then, its structural and transport properties were computationally investigated in detail. The results were compared with the high symmetry $\Sigma5$ $\Sigma11$ $\Sigma13$ GBs, another mixed GB formed by (20−1) and (100) planes and SC systems. In agreement with other computational and experimental studies, at 2300 K, the optimum Y_2O_3 content for maximum oxygen self-diffusion was found to be between 8–11 mol%. Further, it was found that the grain orientations play an essential role in oxygen-ion diffusion. Not only the GB core but also grain interior regions behave differently for different orientations. In contrast to (−511) grain orientations, (21−1) grain has the optimal Y^{3+} distribution, which resulted in (21−1) grain performing even better than the high symmetry GBs. Same behaviour was found for (100) plane for the other mixed GB investigated in this work. Conclusively, ion conductivity through GBs is highly dependent on grain orientations, operating temperature, and Y_2O_3 concentration. Therefore, GBs should be optimized with respect to these parameters in order to design high-efficiency YSZ electrolytes. The GB effect is specifically critical for nanocrystalline samples where the space-charge regions control the ionic conductivity.

Conflicts of interest

There are no conflicts to declare.

Acknowledgements

This research was enabled in part by support provided by Calcul Québec (https://www.calculquebec.ca) and Compute Canada (www.computecanada.ca). The authors acknowledge the Natural Sciences and Engineering Research Council of Canada (NSERC) Discovery grant program, [Funding Reference number RGPIN-2020-05924], Canada Research Chair (CRC) program, and the Canada Foundation for Innovation (CFI) for infrastructure and operating funds. Authors acknowledge the fruitful discussions with Dr Daniele Pergolesi.

References

1 J. F. Marin and P. Contamin, Uranium and oxygen self-diffusion in UO_2, *J. Nucl. Mater.*, 1969, **30**, 16–25.
2 A. C. S. Sabioni, W. B. Ferraz and F. Millot, Effect of grain-boundaries on uranium and oxygen diffusion in polycrystalline UO_2, *J. Nucl. Mater.*, 2000, **278**, 364–369.
3 E. Vincent-Aublant, J. M. Delaye and L. Van Brutzel, Self-diffusion near symmetrical tilt grain boundaries in UO_2 matrix: a molecular dynamics simulation study, *J. Nucl. Mater.*, 2009, **392**, 114–120.
4 K. Govers and M. Verwerft, Classical molecular dynamics investigation of microstructure evolution and grain boundary diffusion in nano-polycrystalline UO_2 Classical molecular dynamics investigation of microstructure evolution and grain boundary diffusion in nano-polycrystalline UO_2, *J. Nucl. Mater.*, 2013, **438**, 134–143.

5 N. R. Williams, M. Molinari, S. C. Parker and M. T. Storr, Atomistic investigation of the structure and transport properties of tilt grain boundaries of UO_2, *J. Nucl. Mater.*, 2015, **458**, 45–55.

6 A. R. Symington, M. Molinari, N. A. Brincat, N. R. Williams and S. C. Parker, Defect segregation facilitates oxygen transport at fluorite UO_2 grain boundaries, *Philos. Trans. R. Soc. A*, 2019, **377**(2152), 20190026.

7 B. Feng, N. R. Lugg, A. Kumamoto, Y. Ikuhara and N. Shibata, Direct Observation of Oxygen Vacancy Distribution across Yttria-Stabilized Zirconia Grain Boundaries, *ACS Nano*, 2017, **11**, 11376–11382.

8 A. L. S. Chua, N. A. Benedek, L. Chen, M. W. Finnis and A. P. Sutton, A genetic algorithm for predicting the structures of interfaces in multicomponent systems, *Nat. Mater.*, 2010, **9**, 418–422.

9 K. S. Chang, Y. F. Lin and K. L. Tung, Insight into the grain boundary effect on the ionic transport of yttria-stabilized zirconia at elevated temperatures from a molecular modeling perspective, *J. Power Sources*, 2011, **196**, 9322–9330.

10 C. A. J. Fisher and H. Matsubara, Oxide ion diffusion along grain boundaries in zirconia: a molecular dynamics study, *Solid State Ionics*, 1998, **113–115**, 311–318.

11 C. A. J. Fisher and H. Matsubara, Molecular dynamics investigations of grain boundary phenomena in cubic zirconia, *Comput. Mater. Sci.*, 1999, **14**, 177–184.

12 C. A. J. Fisher and H. Matsubara, The influence of grain boundary misorientation on ionic conductivity in YSZ, *J. Eur. Ceram. Soc.*, 1999, **19**, 703–707.

13 R. L. González-Romero, J. J. Meléndez, D. Gómez-García, F. L. Cumbrera and A. Domínguez-Rodríguez, A Molecular Dynamics study of grain boundaries in YSZ: structure, energetics and diffusion of oxygen, *Solid State Ionics*, 2012, **219**, 1–10.

14 H. B. Lee, F. B. Prinz and W. Cai, Atomistic simulations of grain boundary segregation in nanocrystalline yttria-stabilized zirconia and gadolinia-doped ceria solid oxide electrolytes, *Acta Mater*, 2013, **61**, 3872–3887.

15 R. L. González-Romero, J. J. Meléndez, D. Gómez-García, F. L. Cumbrera and A. Domínguez-Rodríguez, Segregation to the grain boundaries in YSZ bicrystals: a Molecular Dynamics study, *Solid State Ionics*, 2013, **237**, 8–15.

16 J. An, *et al.*, Atomic scale verification of oxide-ion vacancy distribution near a single grain boundary in YSZ, *Sci. Rep.*, 2013, **3**, 1–6.

17 H. C. Huang, P. C. Su, S. K. Kwak, R. Pornprasertsuk and Y. J. Yoon, Molecular dynamics simulation of oxygen ion diffusion in yttria stabilized zirconia single crystals and bicrystals, *Fuel Cells*, 2014, **14**, 574–580.

18 R. L. González-Romero and J. J. Meléndez, Yttrium segregation and oxygen diffusion along high-symmetry grain boundaries in YSZ, *J. Alloys Compd.*, 2015, **622**, 708–713.

19 S. Zhang, H. Sha, R. H. R. Castro and R. Faller, Atomistic modeling of La^{3+} doping segregation effect on nanocrystalline yttria-stabilized zirconia, *Phys. Chem. Chem. Phys.*, 2018, **20**, 13215–13223.

20 M. Jaipal and A. Chatterjee, Effect of the Σ5(310)/[001] tilt grain boundary on oxygen-ion movement in yttria-stabilized zirconia: Insights from molecular dynamics, *Acta Mater*, 2019, **165**, 307–314.

21 W. Xu, A. Maksymenko, S. Hasan, J. J. Meléndez and E. Olevsky, Effect of external electric field on diffusivity and flash sintering of 8YSZ: a molecular dynamics study, *Acta Mater*, 2020, **206**, 116596.

22 T. Watanabe, Grain boundary engineering: Historical perspective and future prospects, *J. Mater. Sci.*, 2011, **46**, 4095–4115.

23 A. Morawiec and K. Glowinski, On ‘macroscopic’ characterization of mixed grain boundaries, *Acta Mater*, 2013, **61**, 5756–5767.

24 Z. Yu, *et al.*, Segregation-induced ordered superstructures at general grain boundaries in a nickel–bismuth alloy, *Science*, 2017, **358**, 97–101.

25 Z. Luo, *et al.*, A highly asymmetric interfacial superstructure in WC: Expanding the classic grain boundary segregation and new complexion theories, *Mater. Horizons*, 2020, **7**, 173–180.

26 P. V. Nerikar, *et al.*, Grain Boundaries in Uranium Dioxide: Scanning Electron Microscopy Experiments and Atomistic Simulations, *J. Am. Ceram. Soc.*, 2011, **94**, 1893–1900.

27 Y. Pant and B. L. Adams, On the CSL grain boundary distributions in polycrystals, *Scr. Metall. Mater.*, 1994, **30**, 1055–1060.

28 T. Nakagawa, *et al.*, Oxygen diffusion blocking of single grain boundary in yttria-doped zirconia bicrystals, *J. Mater. Sci.*, 2005, **40**(12), 3185–3190.

29 A. Nakamura, *et al.*, Direct Evidence of Dopant-Enhanced Grain-Boundary Sliding in Yttria-Stabilized Zirconia Bicrystals, *J. Am. Ceram. Soc.*, 2005, **88**, 938–942.

30 G. Sánchez-Santolino, *et al.*, Localization of Yttrium Segregation within YSZ Grain Boundary Dislocation Cores, *Phys. status solidi*, 2018, **215**, 1800349.

31 S. Plimpton, Fast Parallel Algorithms for Short-Range Molecular Dynamics, *J. Comput. Phys.*, 1995, **117**, 1–19.

32 D. C. Sayle, S. A. Maicaneanu, B. Slater and C. R. A. Catlow, Exercising control over the influence of the lattice misfit on the structure of oxide–oxide thin film interfaces, *J. Mater. Chem.*, 1999, **9**, 2779–2787.

33 T. X. T. Sayle, C. R. A. Catlow, R. R. Maphanga, P. E. Ngoepe and D. C. Sayle, Generating MnO_2 nanoparticles using simulated amorphization and recrystallization, *J. Am. Chem. Soc.*, 2005, **127**, 12828–12837.

34 L. Minervini, M. O. Zacate and R. W. Grimes, Defect cluster formation in M_2O_3-doped CeO_2, *Solid State Ionics*, 1999, **116**, 339–349.

35 L. Minervini, R. W. Grimes and K. E. Sickafus, Disorder in pyrochlore oxides, *J. Am. Ceram. Soc.*, 2000, **83**, 1873–1878.

36 A. Chroneos, D. Parfitt, J. A. Kilner and R. W. Grimes, Anisotropic oxygen diffusion in tetragonal $La_2NiO_{4+\delta}$: Molecular dynamics calculations, *J. Mater. Chem.*, 2010, **20**, 266–270.

37 D. Parfitt, A. Chroneos, J. A. Kilner and R. W. Grimes, Molecular dynamics study of oxygen diffusion in $Pr_2NiO_{4+\delta}$, *Phys. Chem. Chem. Phys.*, 2010, **12**, 6834–6836.

38 J. Vaari, Molecular dynamics simulations of vacancy diffusion in chromium(III) oxide, hematite, magnetite and chromite, *Solid State Ionics*, 2015, **270**, 10–17.

39 M. O. Zacate, L. Minervini, D. J. Bradfield, R. W. Grimes and K. E. Sickafus, Defect cluster formation in M_2O_3-doped cubic ZrO_2, *Solid State Ionics*, 2000, **128**, 243–254.

40 P. K. Schelling, S. R. Phillpot and D. Wolf, Mechanism of the Cubic-to-Tetragonal Phase Transition in Zirconia and Yttria-Stabilized Zirconia by Molecular-Dynamics Simulation, *J. Am. Ceram. Soc.*, 2001, **84**, 1609–1619.

41 T. Oyama, M. Yoshiya, H. Matsubara and K. Matsunaga, Numerical analysis of solute segregation at Σ5 (310) [001] symmetric tilt grain boundaries in Y_2O_3-doped ZrO_2, *Phys. Rev. B: Condens. Matter Mater. Phys.*, 2005, **71**, 224105.

42 P. P. Ewald, Die Berechnung optischer und elektrostatischer Gitterpotentiale, *Ann. Phys.*, 1921, **369**, 253–287.

43 K. K. Ghuman, E. Gilardi, D. Pergolesi, J. Kilner and T. Lippert, Microstructural and Electronic Properties of the YSZ/CeO_2 Interface *via* Multiscale Modeling, *J. Phys. Chem. C*, 2020, **124**, 15680–15687.

44 M. Chiang, D. P. Birnie and W. D. Kingery, *Physical Ceramics: Principles for Ceramic Science and Engineering*. John Wiley and Sons, Inc., 1996.

45 P. Vonlanthen and B. Grobety, CSL grain boundary distribution in alumina and zirconia ceramics, *Ceram. Int.*, 2008, **34**, 1459–1472.

46 Z. P. Li, T. Mori, G. J. Auchterlonie, J. Zou and J. Drennan, Direct evidence of dopant segregation in Gd-doped ceria, *Appl. Phys. Lett.*, 2011, **98**, 093104.

47 X. Guo and R. Waser, Electrical properties of the grain boundaries of oxygen ion conductors: acceptor-doped zirconia and ceria, *Prog. Mater. Sci.*, 2006, **51**, 151–210.

48 A. R. Symington, M. Molinari, J. Statham, J. Wu and S. C. Parker, The role of dopant segregation on the oxygen vacancy distribution and oxygen diffusion in CeO_2 grain boundaries, *J. Phys. Energy*, 2019, **1**, 042005.

49 P. P. Dholabhai, *et al.*, Structure and segregation of dopant–defect complexes at grain boundaries in nanocrystalline doped ceria, *Phys. Chem. Chem. Phys.*, 2015, **17**, 15375–15385.

50 B. Feng, *et al.*, Atomic structures and oxygen dynamics of CeO_2 grain boundaries, *Sci. Reports*, 2016, **6**(1), 1–7.

51 B. Feng, *et al.*, Atomically ordered solute segregation behaviour in an oxide grain boundary, *Nat. Commun.*, 2016, **7**(1), 1–6.

52 D. Stradi, L. Jelver, S. Smidstrup and K. Stokbro, Method for determining optimal supercell representation of interfaces, *J. Phys. Condens. Matter*, 2017, **29**, 185901.

53 M. Coduri, M. Scavini, M. Allieta, M. Brunelli and C. Ferrero, Defect structure of Y-doped ceria on different length scales, *Chem. Mater.*, 2013, **25**, 4278–4289.

54 S. Grieshammer, B. O. H. Grope, J. Koettgen and M. Martin, A combined DFT + U and Monte Carlo study on rare earth doped ceria, *Phys. Chem. Chem. Phys.*, 2014, **16**, 9974–9986.

55 J. A. Purton, A. Archer, N. L. Allan and D. S. D. Gunn, Growth of nano-domains in Gd–CeO_2 mixtures: hybrid Monte Carlo simulations, *J. Mater. Chem. A*, 2016, **4**, 4592–4602.

56 J. A. Purton, N. L. Allan and D. S. D. Gunn, Simulations of doped CeO_2 at finite dopant concentrations, *Solid State Ionics*, 2017, **299**, 32–37.

57 S. J. Dillon, M. P. Harmer and J. Luo, Grain boundary complexions in ceramics and metals: An overview, *JOM*, 2009, **61**, 38–44.

58 P. R. Cantwell, *et al.*, Grain boundary complexions, *Acta Mater*, 2014, **62**, 1–48.

59 A. R. Krause, *et al.*, Review of grain boundary complexion engineering: know your boundaries, *J. Am. Ceram. Soc.*, 2019, **102**, 778–800.

60 A. A. Valladares, Generating amorphous and liquid aluminum: A new approach, *J. Non. Cryst. Solids*, 2007, **353**, 3540–3544.

61 A. N. Cormack, Mass Transport in Anion Deficient Fluorite Oxides, *Mater. Sci. Forum*, 1986, **7**, 177–186.

62 C. Suciu, E. Dorolti and A. C. Hoffmann, Physico-chemical properties of nanocrystalline YSZ powders as a function of doping level and electrical properties after sintering, *Mater. Sci. Energy Technol.*, 2018, **1**, 136–145.

63 K. C. Lau and B. I. Dunlap, Molecular dynamics simulation of yttria-stabilized zirconia (YSZ) crystalline and amorphous solids, *J. Phys. Condens. Matter*, 2011, **23**, 035401.

64 M. W. Owen, *et al.*, Diffusion in doped and undoped amorphous zirconia, *J. Nucl. Mater.*, 2021, **555**, 153108.

65 M. J. D. Rushton, I. Ipatova, L. J. Evitts, W. E. Lee and S. C. Middleburgh, Stoichiometry deviation in amorphous zirconium dioxide, *RSC Adv*, 2019, **9**, 16320–16327.

66 K. K. Ghuman, E. Gilardi, D. Pergolesi, J. A. Kilner and T. K. Lippert, Microstructural and Electronic Properties of YSZ/CeO_2 Interface *via* Multiscale Modelling, *J. Phys. Chem. C*, 2020, **124**(29), 15680–15687.

67 T. X. T. Sayle, S. C. Parker and D. C. Sayle, Ionic conductivity in nano-scale CeO_2/YSZ heterolayers, *J. Mater. Chem.*, 2006, **16**, 1067–1081.

68 J. An, *et al.*, Atomic Scale Verification of Oxide-Ion Vacancy Distribution near a Single Grain Boundary in YSZ, *Sci. Reports*, 2013, **3**(1), 1–6.

69 R. A. D. Souza, *et al.*, Oxygen diffusion in nanocrystalline yttria-stabilized zirconia : the effect of grain boundaries, *Phys. Chem. Chem. Phys.*, 2008, **10**, 2067–2072.

70 R. A. De Souza, The formation of equilibrium space-charge zones at grain boundaries in the perovskite oxide $SrTiO_3$, *Phys. Chem. Chem. Phys.*, 2009, **11**, 9939–9969.

71 M. De Ridder, *et al.*, Subsurface segregation of yttria in yttria stabilized zirconia, *J. Appl. Phys.*, 2002, **92**, 3056–3064.

72 B. Arndt, *et al.*, Structure and stability of Gd-doped CeO_2 thin films on yttria-stabilized zirconia, *Thin Solid Films*, 2016, **603**, 56–61.

73 N. Shibata, F. Oba, T. Yamamoto and Y. Ikuhara, Grain-Boundary Atomic Structures in Zirconia Ceramics, *Ceramic Engineering and Science Proceedings*, 2008, ch. 16.

74 S. Naoya, F. Obaz, T. Yamamoto and T. Sakuma, Atomic structure and solute segregation of a S = 3, [110]/{111}

grain boundary in an yttria-stabilized cubic zirconia bicrystal, *Philos. Mag. Lett.*, 2002, **82**, 393–400.

75 T. Nakagawa, *et al.*,Oxygen diffusion blocking of single grain boundary in yttria-doped zirconia bicrystals, *J. Mater. Sci.*, 2005, **40**(12), 3185–3190.

76 T. Arima, K. Fukuyo, K. Idemitsu and Y. Inagaki, Molecular dynamics simulation of yttria-stabilized zirconia between 300 and 2000 K, *J. Mol. Liq.*, 2004, **113**, 67–73.

77 W. Araki and Y. Arai, Molecular dynamics study on oxygen diffusion in yttria-stabilized zirconia subjected to uniaxial stress in terms of yttria concentration and stress direction, *Solid State Ionics*, 2010, **181**, 1534–1541.

78 S. H. Guan, C. Shang and Z. P. Liu, Resolving the Temperature and Composition Dependence of Ion Conductivity for Yttria-Stabilized Zirconia from Machine Learning Simulation, *J. Phys. Chem. C*, 2020, **124**, 15085–15093.

79 R. Pornprasertsuk, P. Ramanarayanan, C. B. Musgrave and F. B. Prinz, Predicting ionic conductivity of solid oxide fuel cell electrolyte from first principles, *J. Appl. Phys.*, 2005, **98**, 103513.

80 T. van Dijk and A. J. Burggraaf, Grain boundary effects on ionic conductivity in ceramic $GdxZr_1–xO_2–(x/2)$ solid solutions, *Phys. status solidi*, 1981, **63**, 229–240.

81 O. J. Durá, *et al.*, Ionic conductivity of nanocrystalline yttria-stabilized zirconia: Grain boundary and size effects, *Phys. Rev. B: Condens. Matter Mater. Phys.*, 2010, **81**, 184301.

82 Y. Yamamura, S. Kawasaki and H. Sakai, Molecular dynamics analysis of ionic conduction mechanism in yttria-stabilized zirconia, *Solid State Ionics*, 1999, **126**, 181–189.

83 X. Li and B. Hafskjold, Molecular dynamics simulations of yttrium-stabilized zirconia, *J. Phys. Condens. Matter*, 1995, **7**, 1255–1271.